Event Horizon Telescope
Memo Series

EHT Memo 2017-CE-03

*Calibration & Error Analysis WG*

# Submillimeter Telescope Calibration Memo
# Updated absolute amplitude calibration procedure for 2017

S. Issaoun[1], T. W. Folkers[2], D. P. Marrone[2], J. Kim[2], R. Tilanus[1] and H. Falcke[1]

Oct 1, 2017 – Version 3.0

[1]*Department of Astrophysics/IMAPP, Radboud University Nijmegen, 6500 GL Nijmegen, the Netherlands*
[2]*Arizona Radio Observatory, Steward Observatory, University of Arizona, AZ 85721 Tucson, USA*

Memo history:
- May 26, 2017 – Version 2.0
- Apr 20, 2016 – Version 1.0

**Abstract**

This document presents a step-by-step explanation of the Submillimeter Telescope (SMT) calibration procedure for the antenna-based a priori amplitude calibration as part of the Event Horizon Telescope (EHT). During the EHT+ALMA April 2017 observing run, a number of calibration observations and tests were done. The measurement and reduction processes for each of the SMT a priori calibration deliverables are described in this memo. Improvements to the calibration procedure include: a newly estimated and updated beam-width for the telescope at 228.1 GHz enabling a more accurate estimation of the flux density scaling using planet calibrator observations; a step-by-step outline of the system temperature calibration process using exact equations from the telescope software scripts; tests of various parts of the signal chain for potential amplitude losses; and a newly determined gain curve for 2017.

*Note: This document can be used in conjunction with similar calibration outlines from other stations for procedural comparisons. It contains the most accurate calibration information for the SMT to date and thus renders results from previous memos obsolete.*

# Contents

## Relevant terminology

Relevant variables introduced in this document (brightness temperatures approximated with the Rayleigh-Jeans approximation):

- $C_{\mathrm{hot}}$: Counts measured when looking at the hot load (vane)
- $C_{\mathrm{cold}}$: Counts measured when looking at the cold load (liquid nitrogen)
- $C_{\mathrm{on}}$: Counts measured observing a target
- $C_{\mathrm{sky}}$: Counts measured when looking at blank sky
- $T_{\mathrm{cold}}$: temperature of the cold load
- $T_{\mathrm{rx}}$: receiver noise temperature
- $T_{\mathrm{vane}}$: temperature of the vane (blocker)
- $T_{\mathrm{amb}}$: ambient temperature around the SMT, as measured by the weather station on Mount Graham (physical temperature)
- $T_{\mathrm{em}}$: temperature of the atmospheric emission (also interchangeably called $T_{\mathrm{sky}}$ in the literature, the brightness temperature of the sky)
- $T_{\mathrm{em,i}}$: temperature of the atmospheric emission in the image band (sideband not used for observing)
- $T_{\mathrm{em,s}}$: temperature of the atmospheric emission in the signal band
- $T_{\mathrm{cab}}$: physical temperature of the receiver cabin (this is assumed to be the same as the ambient temperature)
- $T_{\mathrm{cal}}$: derived temperature to give a correct temperature scale for the signal band
- $T_{\mathrm{sys}}$: system noise temperature of the system
- $T^{*}_{\mathrm{sys}}$: effective system noise temperature (corrected for atmospheric attenuation and rearward losses)

Efficiency and correction terms:

- $r_{\mathrm{sb}}$: sideband ratio - since the SMT is a single-sideband receiver, $r_{\mathrm{sb}} = \frac{g_i}{g_s} \ll 1$ since no signal comes from the image band but some leakage can still be present
- AM: amount of airmass in the line of sight of the receiver (elevation-dependent)
- $\tau_0$: atmospheric opacity at the zenith
- $e^{-\tau}$: atmospheric attenuation factor, which damps the signal based on atmospheric opacity in the line of sight $\tau = \tau_0 \times \mathrm{AM}$
- $\tau_{0,s}$: atmospheric opacity at the zenith in the signal band (same principle for image band)
- el: elevation of the antenna dish for a particular observation (in degrees)
- $g(\mathrm{el})$: elevation-dependent gain curve correcting for changing illumination of the main reflector and ground contributions as the dish moves and tilts to different elevations
- $\eta_{\mathrm{l}}$: forward efficiency representing the fraction of power received through the forward atmosphere
- $\eta_{\mathrm{taper}}$: efficiency loss due to non-uniform illumination of the aperture plane by the tapered radiation pattern
- $\eta_{\mathrm{block}}$: aperture blockage efficiency due to blocking of the feed by the sub-reflector (including its support legs)
- $\eta_{\mathrm{spillover}}$: feed spillover efficiency past the main reflector − it is the ratio of the power intercepted by the reflective elements to the total power
- $\eta_{\mathrm{Ruze}}$: surface error efficiency (or Ruze loss) calculated from Ruze's formula (Ruze 1952)
- $\eta_{\mathrm{A}}$: aperture efficiency approximated for the SMT, a combination of various efficiencies ( $= \eta_{\mathrm{taper}} \times \eta_{\mathrm{block}} \times \eta_{\mathrm{spillover}} \times \eta_{\mathrm{Ruze}}$ )
- $\mathrm{A}_{\mathrm{geom}}$: geometric area of the SMT dish
- $\mathrm{A}_{\mathrm{eff}}$: effective area of the SMT dish ( $= \eta_{\mathrm{A}}\mathrm{A}_{\mathrm{geom}}$ )

# 1 Introduction

A telescope's system-equivalent flux density (SEFD) is simply the noise contribution of the system, given by the system noise temperature, and all losses and gains, converted to a flux density scale. The SEFDs can be calculated using system noise temperature $T_{\rm sys}$ measurements and all efficiencies and contributions to source attenuation and noise, and one can determine the sensitivity of the telescope when compared to other telescopes in the array. The higher a telescope's SEFD, the lower its sensitivity. Ultimately, the flux density of a source is simply the telescope's SEFD, which contains all system and telescope parameters and efficiencies, multiplied by the ratio of signal to noise power (defined as $r_{\rm S/N}$) of the source detection. The equation for the SEFD can be subdivided into three main components, each with station-based variations for how they are determined and measured. The three components to the SEFD are:

1. $T_{\rm sys}$: the total noise characterization of the system, given by the system noise temperature
2. $\frac{e^{\tau}}{\eta_{\rm l}}$: the correction terms for attenuation of the source signal by the atmosphere and rearward losses
3. $G$: The antenna gain, including all the loss terms from the telescope and the conversion from a temperature scale (K) to a flux density scale (Jansky), given by the "degrees per flux density unit" factor (DPFU) in K/Jy and the normalized elevation-dependent gain curve $g$(el):
   DPFU $= \frac{\eta_{\rm A} A_{\rm geom}}{2k}$, giving antenna gain $G = {\rm DPFU} \times g({\rm el})$

This gives the following general equation for a telescope's SEFD:

$$\mathrm{SEFD} = \frac{T_{\rm sys} e^{\tau}}{\eta_{\rm l} G} \tag{1}$$

The flux density of a source detected with a given ratio of signal to noise power $r_{\rm S/N}$ is then:

$$S_{\rm source} = \mathrm{SEFD} \times r_{\rm S/N} = \frac{r_{\rm S/N} \times T_{\rm sys} e^{\tau}}{\eta_{\rm l} G} \tag{2}$$

For mm-observatories, which measure the effective system temperature $T^{*}_{\rm sys} = T_{\rm sys} \frac{e^{\tau}}{\eta_{\rm l}}$ directly using the chopper technique[1], the SEFD equation can be rewritten in only two components, the effective system noise temperature and the antenna gain:

$$\mathrm{SEFD} = \frac{T^{*}_{\rm sys}}{G} \tag{3}$$

For the SMT, the SEFD at zenith is of order 13 000 Jansky.

In order to fully calibrate the SMT amplitude scale, we must have a comprehensive understanding of the variables involved in the calculation of source flux densities and how they are measured and obtained. The following equations and descriptions explain the entire procedure for the SMT. In order to easily understand the variables within `LinuxPops`, the SMT in-house calibration software, a compilation of each variable in the theoretical calibration below and its `LinuxPops` counterpart can be found in Appendix A.

# 2 Telescope-specific parameters and efficiencies

The most basic parameter relevant for the sensitivity of a parabolic antenna is its geometrical collecting area, which affects the amount of radiation reflected from the primary onto the secondary reflector. The geometric area of the SMT is calculated with a known diameter of the dish of 10 meters:

$$A_{\rm geom} = \frac{\pi D^2}{4} \approx 78.54 \ {\rm m}^2 \tag{4}$$

The aperture efficiency represents the efficiency of the telescope compared to a telescope with a perfect collecting area (uniform illumination, no blockage or surface errors) and it is determined using observations of known calibrator sources, usually planets. It corrects for the forward losses of the telescope during observing. We can write the aperture efficiency as the combination of various efficiency terms:

$$\eta_{\rm A} = \eta_{\rm taper} \times \eta_{\rm block} \times \eta_{\rm spillover} \times \eta_{\rm Ruze} \tag{5}$$

Each efficiency term corresponds to an aspect of the telescope feed:[2]

- $\eta_{\rm taper}$ is the efficiency loss due to non-uniform illumination of the aperture plane by the tapered radiation pattern/feed function (also formally known as the illumination efficiency). It is the most important contributor to the aperture efficiency.

[1] See the complementary *A priori Calibration Memo* by Issaoun et al. (2017) for details

[2] See Baars, J., *The paraboloidal reflector antenna in radio astronomy*, Springer, 2007 for more detail on the measurement of the different losses.

- $\eta_{\rm block}$ is the aperture blockage efficiency due to blocking of the feed by the sub-reflector (including its support legs)

- $\eta_{\rm spillover}$ is the feed spillover efficiency past the main reflector - it is the ratio of the power intercepted by the reflective elements beyond the edge of the primary and the sub-reflector to the total power. It is due partly to cold sky and partly to a warm background, and is elevation-dependent.

- $\eta_{\rm Ruze}$ is the surface error efficiency (also called "Ruze loss" or scattering efficiency) calculated from Ruze's formula (Ruze 1952). It is due to randomly distributed small-scale deviations of the reflector from the perfect paraboloidal shape. Ruze's formula is presented below, where $\sigma$ is the surface rms (accounting for small-scale deviations from a perfect surface through dish holography) and $\lambda$ is the observing wavelength:

$$\eta_{\rm Ruze}(\lambda) = e^{\frac{-16\pi^2\sigma^2}{\lambda^2}} \tag{6}$$

Additionally, telescopes do not have perfect surfaces, and must thus suffer some losses and gains of signal due to distorted illumination of the main reflector as they slowly move to different elevations. This large-scale surface deformation affects the received signal and is not taken into account in the general aperture efficiency calculation. These losses however can be determined by tracking sources through a wide range of elevations, and thus measure an elevation-dependent gain curve for the telescope, where the maximum ($g = 1$) is set where the telescope is expected to be the most efficient. This normalized gain curve is usually written in the form of a second order polynomial (in the standard VLBA format), where 'el' is the elevation in degrees:

$$g(\mathrm{el}) = a_2(\mathrm{el})^2 + a_1(\mathrm{el}) + a_0 \tag{7}$$

An updated gain curve for 2017 can be found in Section 8.

# 3 The SMT DPFU

We have previously defined the antenna gain as a combination of the telescope's DPFU and its normalized elevation-dependent gain curve. To obtain the SMT's Jy/K factor $f_{\rm Jy/K}$, independent of elevation, we simply take the inverse of the DPFU:

$$\mathrm{DPFU} = \frac{A_{\rm geom}\eta_{\rm A}}{2k}\ [\mathrm{K/Jy}] \tag{8}$$

$$f_{\rm Jy/K} = \frac{1}{\mathrm{DPFU}} = \frac{2k}{A_{\rm geom}\eta_{\rm A}}\ [\mathrm{Jy/K}] \tag{9}$$

The antenna gain will of course also be affected by the gain curve, not included in $f_{\rm Jy/K}$, depending on the elevation of the observed source. A time-dependent DPFU can also be estimated using flux measurements of planets at different times during the observing window.

## 3.1 The SMT beam-width

In order to confidently provide an aperture efficiency for the telescope, a reliable beam-width must be used. The expected flux densities from calibrators are dependent on the coupling of the source size to the telescope beam. Therefore an accurate estimation of the telescope beam-width is a necessary input for the simulation programs giving expected calibrator fluxes.

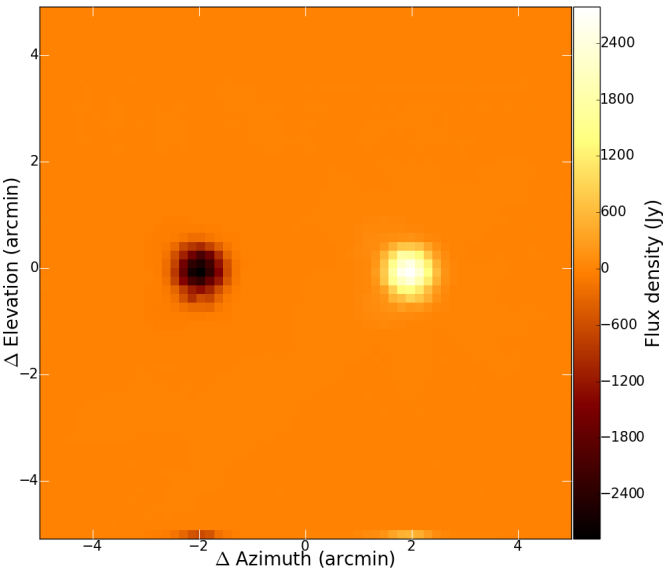


Figure 1: The 5′ by 5′ az-el continuum grid map of Jupiter taken on 11 April, 2017. On the left side is the image of Jupiter mapped by the negative beam and on the right side is the image of Jupiter mapped by the positive beam.

After the EHT+ALMA run in April 2017, we made a continuum map of Jupiter to estimate the telescope beam-width at the EHT observing frequency (228.1 GHz). The map is a 5′ by 5′ azimuth-elevation (az-el) grid map, with the telescope moving horizontally in azimuth at each elevation increment of 10″. The map is shown in Fig. 1. The SMT has a chopping beam with a separation of 4′ between the two beams: during

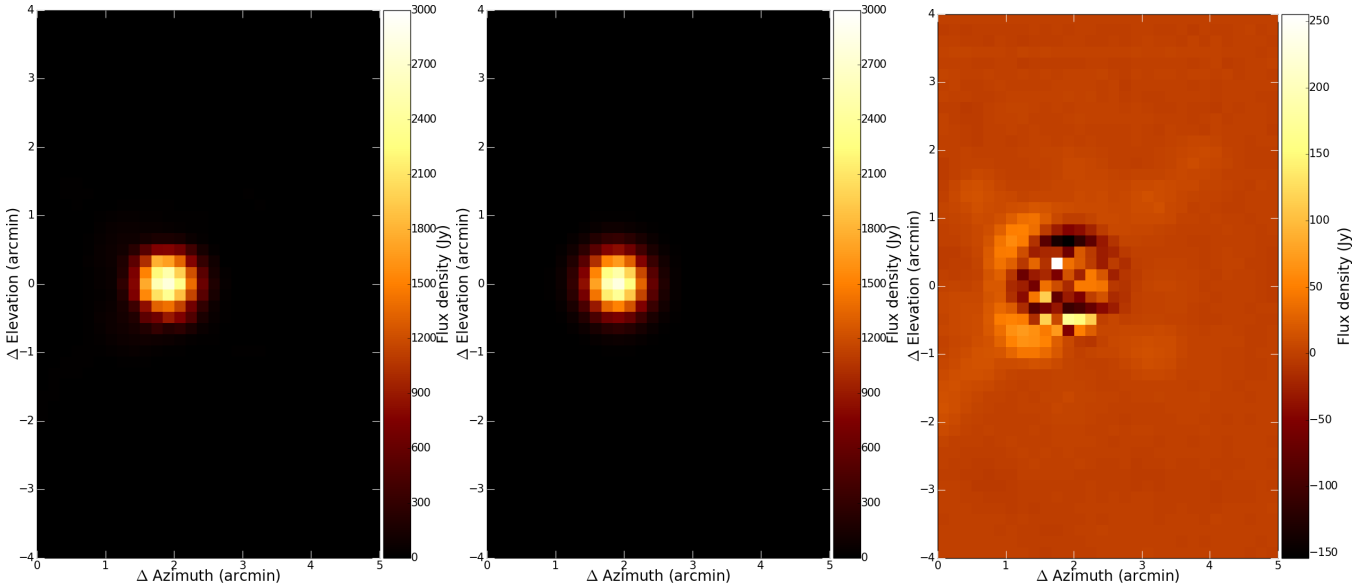


Figure 2: *Left:* Map of Jupiter by the positive beam of the SMT. *Center:* Best-fit 2D Gaussian model of the positive beam map. *Right:* Residual map of the model-subtracted image.

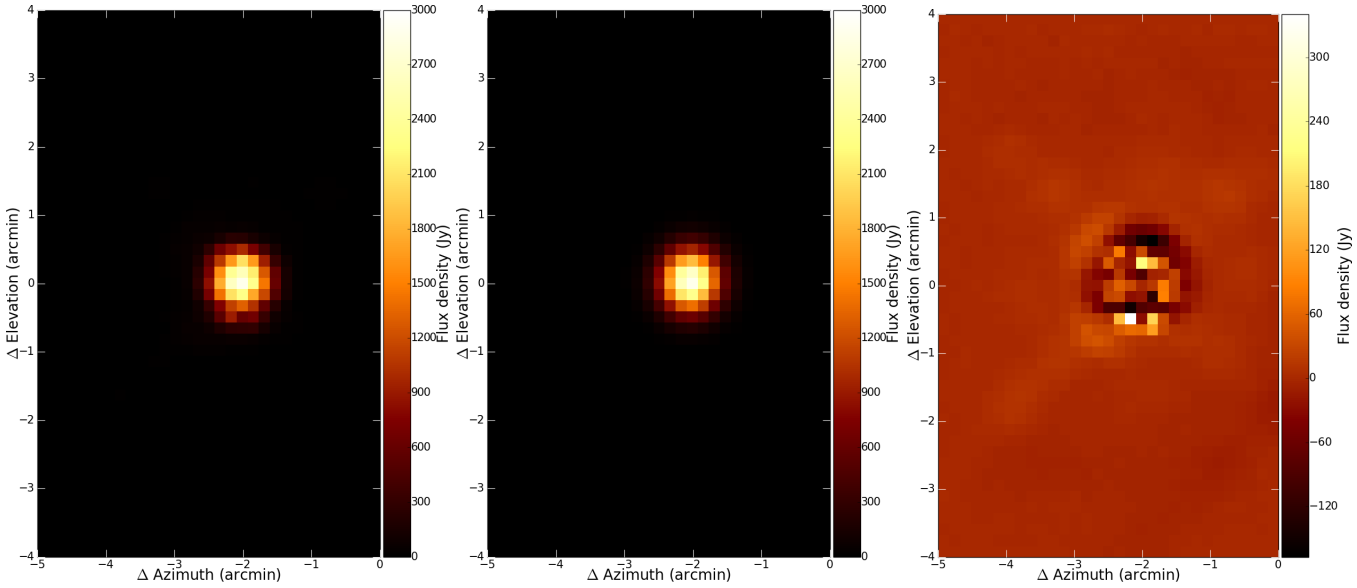


Figure 3: *Left:* Map of Jupiter by the negative beam of the SMT. *Center:* Best-fit 2D Gaussian model of the negative beam map. *Right:* Residual map of the model-subtracted image.

the az-el grid mapping, both the negative and positive beam slew through the map area, hence the two images of Jupiter.

A first attempt at obtaining the beam-width of the telescope was made by fitting a Gaussian to the flux density collected by the telescope at the zero elevation change mark, along the azimuth change. The deconvolution of the beam-width $\theta_{\rm mb}$ (the width of the main lobe of the telescope beam pattern) from the full width at half-maximum (FWHM) of a Gaussian is estimated as follows (accurate to about 2% for an extended source). The diameter of Jupiter $\theta_{\rm Jupiter} = 41.17''$, as computed from the Planet program for 11 April 2017, was used for the deconvolution. The beam-width is thus given by:

$$\theta_{\rm mb} = \sqrt{\rm FWHM^2 - \frac{\ln(2)}{2}\theta^2_{\rm Jupiter}} \qquad (10)$$

This method gave wildly varying beam-widths between the positive and negative beam. Therefore, a different analysis was used for a more robust result: using a least-squares fit of a 2D Gaussian model for each beam window. Since the noise level is near zero, the fits were done without subtraction of a background.

A 2D Gaussian model was fitted to both the negative and positive beam images of Jupiter, and then the telescope beam size was deconvolved from the resulting FWHM in the azimuth and elevation directions and the known diameter of Jupiter on April 11, 2017, as previously outlined in Eq. 10. Fig. 2 and Fig. 3 show the best-fit 2D Gaussian model for the Jupiter images taken by the positive and negative beams of the SMT respectively. Table 1 presents the dimensions of the telescope beams estimated from the 2D Gaussian fits.

Table 1: Measured beam-widths from the Jupiter az-el grid map using 2D Gaussian fits for the positive and negative beam.

| Beam | Beam-width along ΔAz [arcseconds] | Beam-width along ΔEl [arcseconds] |
|---|---|---|
| Positive | 36.1 ± 0.3 | 34.9 ± 0.3 |
| Negative | 32.6 ± 0.3 | 35.4 ± 0.3 |

Of course this method only gives a simple fit, but this should be sufficient for the analysis of the telescope DPFU, in particular because other uncertainties dominate (pointing, focus). The difference between the sizes of the positive and negative beams are not yet fully understood, but it is possibly caused either by technical differences in the chopping of the secondary between the two beams or by non-uniform illumination of the dish from distortions on the surface of the main reflector. The latter is also further shown by the non-symmetrical distortions caused by the secondary support legs, as shown in Fig. 4.

This is also supported by the fact that the residuals of the model-subtracted images from the two beams are not mirror images of each other but are both biased to the left side: this again points toward asymmetry in dish illumination. Asymmetry between the two beams is also not an uncommon phenomenon for radio-telescopes with the same chopping setup. Other possible effects could be atmospheric distortions, tracking errors or gridding problems during the mapping (the az-el grid map mode is not used frequently at the SMT).

From Table 1 we can estimate an average beam-width for the SMT at 228.1 GHz: $\theta_{\mathrm{SMT}} = 34.8 \pm 0.6$ arcseconds. It is important to note however that an approximation of a circular beam might not be entirely accurate for the SMT, as Table 1 shows. However, any uncertainty from the beam-width used will not be the dominating factor for the uncertainty in the DPFU, making the average estimate an adequate value to use for the calibration procedure.

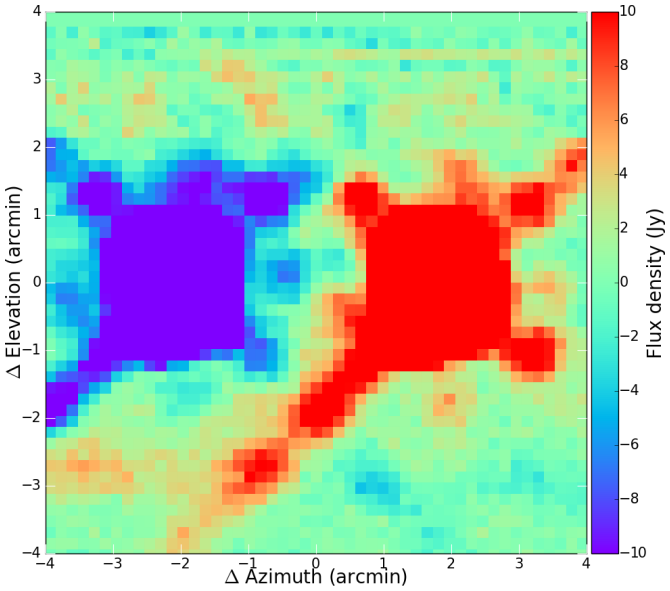


Figure 4: Map of Jupiter with a smaller flux density range enables the viewing of the spillage from the secondary reflector support legs for each beam.

## 3.2 The aperture efficiency

With the newly updated telescope beam-width, the aperture efficiency for the SMT can now be estimated from planet observations. We have decided not to use the SMT in-house `Planet` simulation software for the following calculations (as was usually done in past memos) but to instead only use the brightness temperatures and apparent sizes given for Saturn, Jupiter and Mars and calculate every step of the calibration independently. The newly estimated aperture efficiencies with the method described here render measurements in past memos outdated and innacurate.

The observed planet fluxes from the SMT calibrator scans are compared to expected planet flux densities in the telescope beam for a perfect telescope at the given frequency and beam-width. The aperture efficiency $\eta_{\mathrm{A}}$ is found using the following equation, where $T_{\mathrm{A}}^{*}$ is the observed effective antenna temperature, $g$(el) is the telescope gain curve, $k$ is the Boltzmann constant, $A_{\mathrm{geom}}$ is the geometric area of the telescope and $S_{\mathrm{beam,sim}}$ is the expected flux density of the planet in the telescope beam estimated from planet information such as

apparent size and brightness temperature:

$$\eta_{\mathrm{A}} = \frac{2k}{A_{\mathrm{geom}}} \frac{T_{\mathrm{A}}^{*}}{g(\mathrm{el}) S_{\mathrm{beam,sim}}} \tag{11}$$

Or similarly the DPFU is directly given by:

$$\mathrm{DPFU} = \frac{T_{\mathrm{A}}^{*}}{g(\mathrm{el}) S_{\mathrm{beam,sim}}} \tag{12}$$

For extended sources, it is important to calibrate the flux density observed in the beam because some emission might not be picked up by the telescope. The aperture efficiency is only concerned by the main beam flux density, and so the following equation is used to calibrate the simulated flux density in the beam for an extended source, where $S_{\mathrm{sim}}$ is the expected total flux density of the source:

$$S_{\mathrm{beam,sim}} = S_{\mathrm{sim}} \times K \tag{13}$$

$K$ is determined by the following equation, where $\theta_{\mathrm{mb}}$ is the half-power beam-width in arcseconds of the primary lobe of the telescope beam pattern (telescope beam diameter) and $\theta_{\mathrm{s}}$ is the diameter in arcseconds of the observed extended source:

$$x = \frac{\theta_{\mathrm{s}}}{\theta_{\mathrm{mb}}} \sqrt{\ln(2)} \tag{14}$$

$$K = \frac{1 - e^{-x^2}}{x^2} \tag{15}$$

This $K$ factor is the ratio of the beam-weighted source solid angle and the solid angle of the source on the sky. It is in fact the integral of the antenna pattern of the telescope (approximated as a normalized gaussian) $P(\theta, \phi) = e^{-\ln 2 (2\theta/\theta_{\mathrm{mb}})^2}$ and a disklike source with a uniform brightness distribution $\Psi(\theta, \phi) = 1$ over the size of the extended source. This serves very well for our a priori calibration purposes.

$$K = \frac{\Omega_{\mathrm{sum}}}{\Omega_{\mathrm{s}}} = \frac{1}{\Omega_{\mathrm{s}}} \int_{\mathrm{source}} P(\theta - \theta', \phi - \phi') \Psi(\theta', \phi') d\Omega' \tag{16}$$

$$K = \frac{1}{\Omega_{\mathrm{s}}} \int_{\mathrm{source}} P(\theta - \theta', \phi - \phi') d\Omega' \tag{17}$$

The expected total flux density is estimated by:

$$S_{\mathrm{sim}} = \frac{2h}{c^2} \frac{\nu^3 \Omega_{\mathrm{s}}}{e^{\frac{h\nu}{kT_{\mathrm{B}}}} - 1}, \tag{18}$$

where $\nu$ is the observing frequency in Hz, $h$ is the Planck constant, $c$ is the speed of light (in m/s), $T_{\mathrm{B}}$ is the mean brightness temperature for the planet (assuming a disk of uniform temperature), and $\Omega_{\mathrm{s}}$ is the solid angle of the source on the sky in steradians. Since we are dealing with very small objects, the latter can be approximated using the small angle approximation, where $\theta_{\mathrm{s}}$ is the apparent diameter of the planet observed, in radians:

$$\Omega_{\mathrm{s}} \simeq \frac{\pi \theta_{\mathrm{s}}^2}{4} \tag{19}$$

Of course this process heavily depends on assumptions made in the planet calibration, such as accurate predicted planet fluxes, stable weather conditions and a well-calibrated instrument in terms of pointing and focus.

For the SMT, the `Planet` program provided brightness temperatures $T_{\mathrm{B}}$ and apparent angular sizes of each planet at a given date and frequency. The program gave, for each planet and each day, a major and minor axis estimation for the planet disk. We approximated the diameter of the planet $\theta_{\mathrm{s}}$ for the flux density calculation as the mean of the major and minor diameters. Table 2 shows typical parameters of planet calibrators for EHT observing at the SMT.

Table 2: Typical planet apparent sizes, brightness temperatures and $K$ correction factors for EHT observing at the SMT over the past three years (for Mars, April 2016 only).

| Planet | $\theta_{\mathrm{s}}$ [arcseconds] | $T_{\mathrm{B}}$ [K] | $K$ factor |
|---|---|---|---|
| Mars | 12 ± 1 | 208 | 0.96 |
| Jupiter | 42 ± 3 | 170 | 0.63 |
| Saturn | 16 ± 2 | 150 | 0.93 |

Planet scans during three EHT observing windows, in 2015, 2016 and 2017, were taken to estimate an aperture efficiency per scan. The measurements with Saturn were discarded due to the Saturn rings influencing the disk approximation for the planet and the need for a more detailed brightness distribution model for accurate estimates of an aperture efficiency. Furthermore, only antenna temperature measurements done in upper sideband (USB) were kept for the analysis, as this is the sideband used for EHT observing. Separate aperture efficiency measurements were also determined per polarization (RCP and LCP). Fig. 5 shows the measurements used for the analysis and the resulting mean aperture efficiency for the SMT.

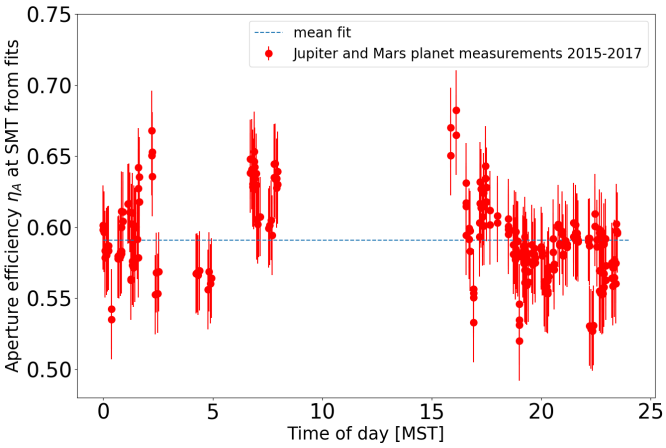


Figure 5: Aperture efficiency estimates for upper sideband measurements (USB) using Jupiter and Mars (2015-2017). The blue dashed line represents the mean aperture efficiency from the measurements. The error bars are estimated from the standard deviation from the mean of the measurements approximated as a Gaussian distribution.

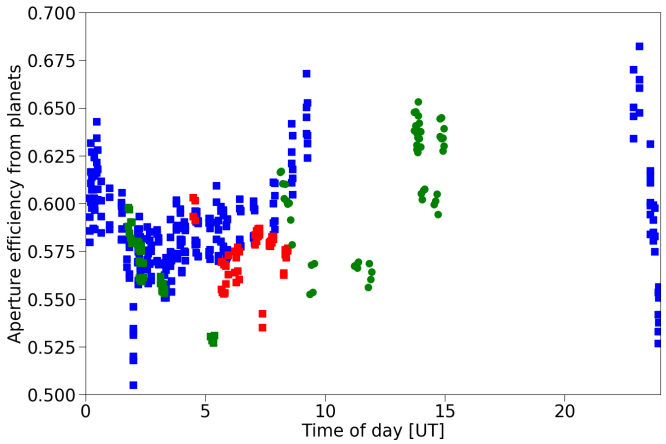


Figure 6: Aperture efficiency estimates using Jupiter (squares) and Mars (circles). 2015 points in blue, 2016 in green and 2017 in red.

An attempt was also made to determine a time-dependent variation of the aperture efficiency as a function of UT time, as shown in Fig. 6. A time-dependence of the aperture efficiency can be caused by the dish being affected by the Sun and heating up during daytime hours, thus reducing telescope sensitivity and efficiency. However, a very peculiar physical trend was observed at the SMT as a function of UT time (local time is in MST = UT − 7). It appears that the telescope is at its most efficient during mid-day and reaches a minimum in the night. The current measurements, which appear to show an increase in efficiency during daytime hours, are not trusted.

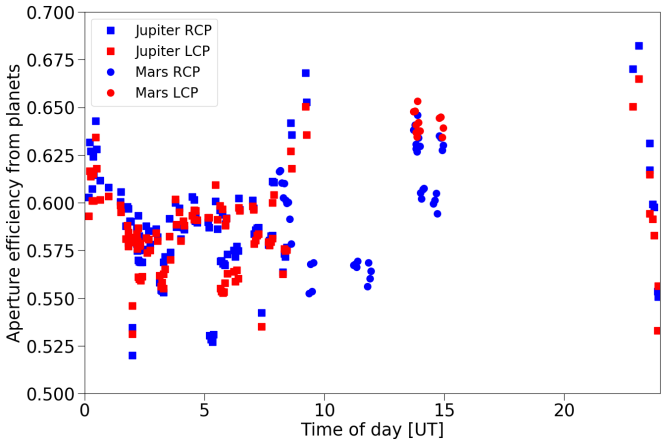


Figure 7: Aperture efficiency measurements separated by polarization: blue is LCP, red is RCP. Once again, the squares are Jupiter and circles are Mars measurements.

The lack of a trusted physical trend for the time-dependence of the aperture efficiency thus led to the conclusion that a single average aperture efficiency must be adopted for the SMT until this behavior can be better understood or a better sampling of planet measurements (not just during EHT weeks in April) can be obtained. The telescope is not particularly known to be under-performing or having difficulties observing in daytime conditions.

The aperture efficiency of the SMT is determined by taking the mean of all aperture efficiency measurements from all three EHT observing windows, and the error on the measurement is the standard deviation determined from the scatter of the measurements around the mean value. It is likely that the error on the aperture efficiency is overestimated, as the scatter of the measurements can be caused by various other effects such as the unsolved time-dependent trend, uncertainties and fluctuations in the measurement of the effective system temperature $T^*_{\rm sys}$ (used to calibrate counts on source to $T^*_{\rm A}$ scale), changes in pointing and focus accuracy or a variable atmosphere due to sparse cloud cover and high winds. In particular, the uncertainty in the $T^*_{\rm sys}$ measurement is also present in the SEFD calculation for the telescope, thus it is likely that its error contribution is double-counted: once for the actual $T^*_{\rm sys}$ values needed to calculate the SEFDs; and once again for their effect on the $\eta_{\rm A}$ measurements.

The mean aperture efficiency and DPFU (or Kelvin-to-Jansky

[3]More digits for the measurements can be obtained upon request.

factor $f_{\mathrm{Jy/K}}$) for the SMT are thus[3]:

$$\eta_{\mathrm{A}} = 0.59 \pm 0.03 \tag{20}$$

$$\mathrm{DPFU} = \frac{\eta_{\mathrm{A}} A_{\mathrm{geom}}}{2k} = 0.0168 \pm 0.0008\ [\mathrm{K/Jy}] \tag{21}$$

$$f_{\mathrm{Jy/K}} = \frac{2k}{\eta_{\mathrm{A}} A_{\mathrm{geom}}} = 59 \pm 3\ [\mathrm{Jy/K}] \tag{22}$$

Furthermore, the difference between RCP and LCP aperture efficiency (or DPFU) was not found to be significant. This can be seen in Fig. 7 for individual measurements and in Figs. 8 and 9 for the mean distributions of aperture efficiency measurements for RCP and LCP respectively.

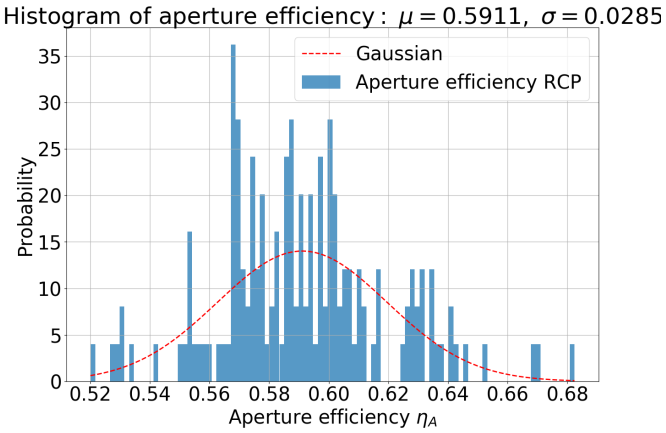


Figure 8: Aperture efficiency distribution for RCP approximated by a Gaussian fit of a mean $\eta_{\mathrm{A,RCP}} = 0.5911$ and a standard deviation of $\sigma_{\mathrm{RCP}} = 0.0285$.

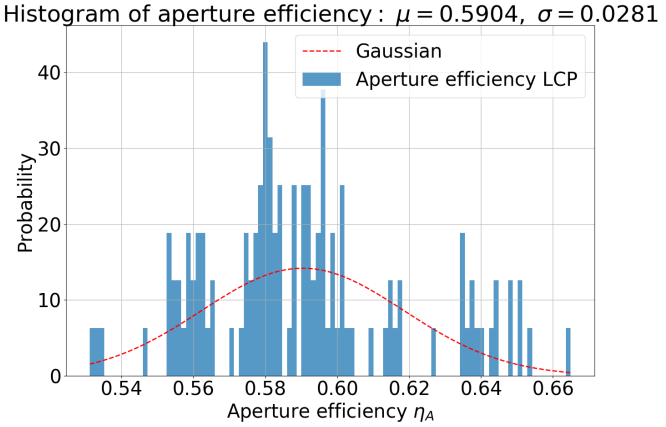


Figure 9: Aperture efficiency distribution for LCP approximated by a Gaussian fit of a mean $\eta_{\mathrm{A,LCP}} = 0.5904$ and a standard deviation of $\sigma_{\mathrm{LCP}} = 0.0281$.

# 4 System noise temperature

The first step to calibrating the flux density measurements of various sources is to determine the noise temperature of the system when the telescope is pointed off-source (blank sky). At the SMT, this is done with the chopper method, by getting a system-to-background ratio of the signal, comparing the power obtained when the telescope is pointed to the sky directly (off-source counts), and when the receiver is blocked by an absorber (chopper counts), and then calibrated to a temperature scale. The following is an account of the exact equations used in the telescope software to determine the effective system noise temperature and other calibration information.[4] A more general approximate procedure can be found in the complementary *A priori Calibration Memo* by Issaoun et al. (2017).

During a cold load calibration with a liquid nitrogen bath (hereby referred to as "cold cal"), the Y-factor and the receiver noise temperature are computed. This is done once every few hours by the operator to refresh receiver noise temperature values. They do not vary much between cold cals:

$$Y = \frac{C_{\mathrm{hot}}}{C_{\mathrm{cold}}}, \tag{23}$$

where the numerator is $C_{\mathrm{hot}}$, the counts obtained from the vane (chopper), and the denominator is $C_{\mathrm{cold}}$, the counts obtained from the cold load (liquid nitrogen bath). The Y-factor also enables an easy diagnostic of the sensitivity of the receiver. A high Y-factor means little receiver noise, and thus sensitive observations (of course what constitutes "high" depends on the type of receiver and the observing frequency). For the SMT, the Y-factor is typically $\sim 2.5$ for EHT observing. Then the cold cal routine calculates the receiver noise temperature as follows:

$$T_{\mathrm{rx}} = \frac{T_{\mathrm{vane}} - Y T_{\mathrm{cold}}}{Y - 1} \tag{24}$$

Here temperatures are used, where $T_{\mathrm{vane}}$ is the temperature of the vane blocker (chopper; at room temperature $\sim$ 290 K) and $T_{\mathrm{cold}}$ is the cold load temperature (for the SMT it is the temperature of liquid nitrogen $\sim$ 77 K).

Then the routine computes an estimate for $T_{\mathrm{em}} = T_{\mathrm{sky}}$, the atmospheric emission temperature (or equivalently the sky

[4]Note: The SMT calibration script written by Thomas Folkers uses the ATM program, a sky emissivity correlation model of sky temperature part of the `ASTRO` package of the `GILDAS` software by IRAM. For more detail on this procedure, see *Calibration of spectral line data at the IRAM 30m radio telescope* by C. Kramer.

brightness temperature), which is later corrected in an iterative process with the ATM program to determine $T^*_{\rm sys}$:

$$T_{\rm em} = T_{\rm vane} - \frac{C_{\rm hot} - C_{\rm sky}}{C_{\rm hot} - C_{\rm cold}}(T_{\rm vane} - T_{\rm cold}) \quad (25)$$

Here $C_{\rm sky}$ corresponds to the counts obtained by looking at blank sky. When the calibration routine is not a cold cal (but is instead a $T^*_{\rm sys}$ routine before a scan/pointing/focus), the program uses the following to estimate $T_{\rm em}$:

$$T_{\rm em} = (T_{\rm rx} + T_{\rm vane})\frac{C_{\rm sky}}{C_{\rm hot}} - T_{\rm rx} \quad (26)$$

The program then iteratively corrects $T_{\rm em}$ using the ATM program to determine the variables in the separate sidebands (signal and image). The atmospheric model (ATM) is used to fit the emission of both sidebands to the sky temperature $T_{\rm em}$ by varying the amount of water vapor. The model uses a standard atmosphere and radiative transfer to compute the total absorption and thermal emission by water vapor and oxygen through the atmosphere. After running the ATM transmission routines for the two sidebands, the atmospheric emission temperature for the image band is computed and simplified as follows:

$$T_{\rm em,i} = \frac{T_{\rm em,s} + r_{\rm sb} \times T_{\rm em,i}}{1 + r_{\rm sb}} + T_{\rm cab} = T_{\rm em,s} \quad (27)$$

With the assumption on the sideband ratio ($r_{\rm sb} = 0$ for single-sideband (SSB) receiver) and the fact that the cabin temperature is computed as $T_{\rm cab} = 0.8T_{\rm vane} + 0.2T_{\rm amb} = 0.8T_{\rm amb} + 0.2T_{\rm amb} = T_{\rm amb}$, the atmospheric emission temperatures in the image band and signal band are equal[5]. This of course depends on the atmospheric absorption spectrum but remains a fair assumption for the Event Horizon Telescope observing frequencies.

Then the program proceeds to compute the calibration temperature $T_{\rm cal}$, which gives the temperature scale for the signal band:

$$\begin{aligned} T_{\rm cal} &= (1.0 + r_{\rm sb})(T_{\rm vane} - T_{\rm em,i})e^{\tau_{0,s} \times AM} \\ &= (T_{\rm vane} - T_{\rm em,i})e^{\tau_{0,s} \times AM} \end{aligned} \quad (28)$$

The opacity at the zenith in the signal band $\tau_{0,s}$ comes from the ATM program, as does the atmospheric emission temperature in the image band $T_{\rm em,i}$. The program uses elaborate equations to compute the airmass, designed for low-elevation observing. These equations will not be explained here, but they do not deviate from the standard AM= $1/\sin(\rm el)$ equation until below 15° (at 15° it deviates by less than 1%).

The calibration temperature represents the difference between the temperature of the sky and the temperature of the vane, corrected for atmospheric losses, determined by the ATM program. In the standard chopper calibration technique, $T_{\rm cal} \sim T_{\rm hot}$. It is important to note that the exponential term here is highly misleading. The presence of this term in $T_{\rm cal}$ serves to stabilize fluctuations in $T_{\rm cal}$ coming from changes in the atmospheric emission temperature with opacity and elevation. It is NOT the cause of the atmospheric correction factor from the chopper technique resulting in the measurement of $T^*_{\rm sys}$. Actual values for $T_{\rm cal}$ are very stable, fluctuate only by 1-2%, and do not change as a function of airmass.

Then the program calculates the effective system temperature (including the atmospheric attenuation correction) $T^*_{\rm sys}$ in the following way:

$$T^*_{\rm sys} = \frac{C_{\rm sky}}{C_{\rm hot} - C_{\rm sky}} T_{\rm cal} \quad (29)$$

The chopper technique determines a system temperature including all noise contributions from the receiver until the top of the atmosphere. Thus, the temperature it outputs is the effective system noise temperature $T^*_{\rm sys}$ , which, when applied to source measurements, would already correct for the source signal attenuation by the atmosphere. This is measured before every scan on a target. In VLBI mode, the quarter wave-plate is added to the signal chain, but since $T^*_{\rm sys}$ is measured before every scan in VLBI mode, the chopper calibration is done with the quarter wave-plate in place. Thus any losses induced by the quarter wave-plate would be corrected via the chopper calibration and will be offset within the $T^*_{\rm sys}$ measurement.

# 5 Obtaining the flux density of a source

We define the antenna temperature for each source measurement, using the signal-to-noise ratio of each measurement, as:

$$T^*_{\rm A} = \frac{C_{\rm on} - C_{\rm sky}}{C_{\rm sky}} T^*_{\rm sys} \quad (30)$$

[5]The assumption that the vane temperature is the same as the ambient/outdoor temperature is no longer trusted. The vane was moved from the receiver cabin to a room in the telescope building, and so the vane temperature is likely closer to room temperature. This is an outstanding issue of the $T^*_{\rm sys}$ calibration.

Notice the (*) symbol: this is because this antenna temperature is corrected for atmospheric absorption, implicitly included in $T^*_{\rm sys}$.

Now correcting for the aperture efficiency and the gain curve as a function of elevation:

$$T_{\rm R} = \frac{T^*_{\rm A}}{\eta_{\rm A} g({\rm el})} \tag{31}$$

$T_{\rm R}$ is the final antenna temperature: it contains all corrections for efficiency and telescope parameter terms, and is thought to be the equivalent of the temperature of a resistor held directly in front of the receiver. Thus, it should account for every telescope-specific and source-specific variables, apart from the conversion to a flux density.

The final step is to convert the temperature scale into a flux density scale in Jansky, where $k = 1.38 \times 10^{-23}$J/K $= 1.38 \times 10^{3}$Jy/K is the Boltzmann constant:

$$S = \frac{2k}{A_{\rm geom}} T_{\rm R} = \frac{8k}{\pi D^2} \frac{T^*_{\rm A}}{\eta_{\rm A} g({\rm el})} \tag{32}$$

# 6 Sky opacity at the SMT

The sky opacity for a particular air mass (AM) changes depending on the elevation of the dish as shown below, where $\tau_0$ is the sky opacity at the zenith:

$$\tau = \tau_0 \times {\rm AM} \tag{33}$$

The opacity at the SMT is measured by a tipping radiometer, which is placed about 100° away from the dish, on the telescope building itself. The SMT building is on a rotating platform, therefore the opacity is not measured through a constant water vapor column but rotates to measure 100° from the target source Azimuth.

In particular, this becomes problematic when the telescope observes targets at 200-210° Azimuth, as the tipper is pointed right at the Large Binocular Telescope (LBT). The warm air and reflection from the LBT building causes abnormal spikes in the tipper opacity readings, and these readings become unreliable and not representative of observing conditions.

Furthermore, in order to correct $T_{\rm cal}$ for atmospheric attenuation, the ATM program uses an iterative linear fit process to determine an opacity, using weather conditions obtained from the Mount Graham weather station, and can deem a tipper reading as "unreliable" if the measured opacity does not match that outputted by the ATM program. That value is then not used for the calculation of the effective system noise temperature, and it instead uses the last good tipper value to compute this. The ATM program then computes the opacity in the signal band in the line of sight at the exact observing frequency using an iterative process, with the tipper opacity and other parameters from the Mount Graham weather station as inputs.

# 7 Signal loss in the VLBI backend

When calibrating VLBI data using individual telescope parameters and calibration information, there may be discrepancies in the instrumental setups for the observing run and the calibration procedures. Since calibration information is usually obtained via the telescope's in-house system, there may be some additional unaccounted effects in the recorded VLBI data as it is obtained through the separate VLBI backend (R2DBEs, Mark6 recorders and modules).

In April 2017, we attempted to constrain possible losses through the VLBI backend using a Y-factor test. This was done by measuring and comparing the Y-factor (ratio between a hot/ambient load and a cold load, see Eq. 23) obtained at the receiver total-power box (part of the SMT setup) and inside the R2DBE itself (R2DBE output[6]).

A spectral analyzer was used for the total-power box and R2DBE input to compare the results directly with the Y-factor measurements outputted by the R2DBE. It was found that the Y-factors at the receiver total-power box and at the VLBI backend, shown for RCP and LCP for both the high and low bands in Fig. 10, are compatible. It is therefore safe to assume that there is no obvious signal loss through to the R2DBE backend that is unaccounted for in the standard amplitude calibration described in this memo for EHT data taken at the SMT from 2015 onward.

Before 2015, the SMT used the R1DBE backend, where no Y-factor test was done, so it remains difficult to account for possible signal losses in older datasets.

[6]This was done using the LMT scripts `collect_mark6_data.py` and `genYSFactor.py` written by L. Blackburn and K. Bouman.

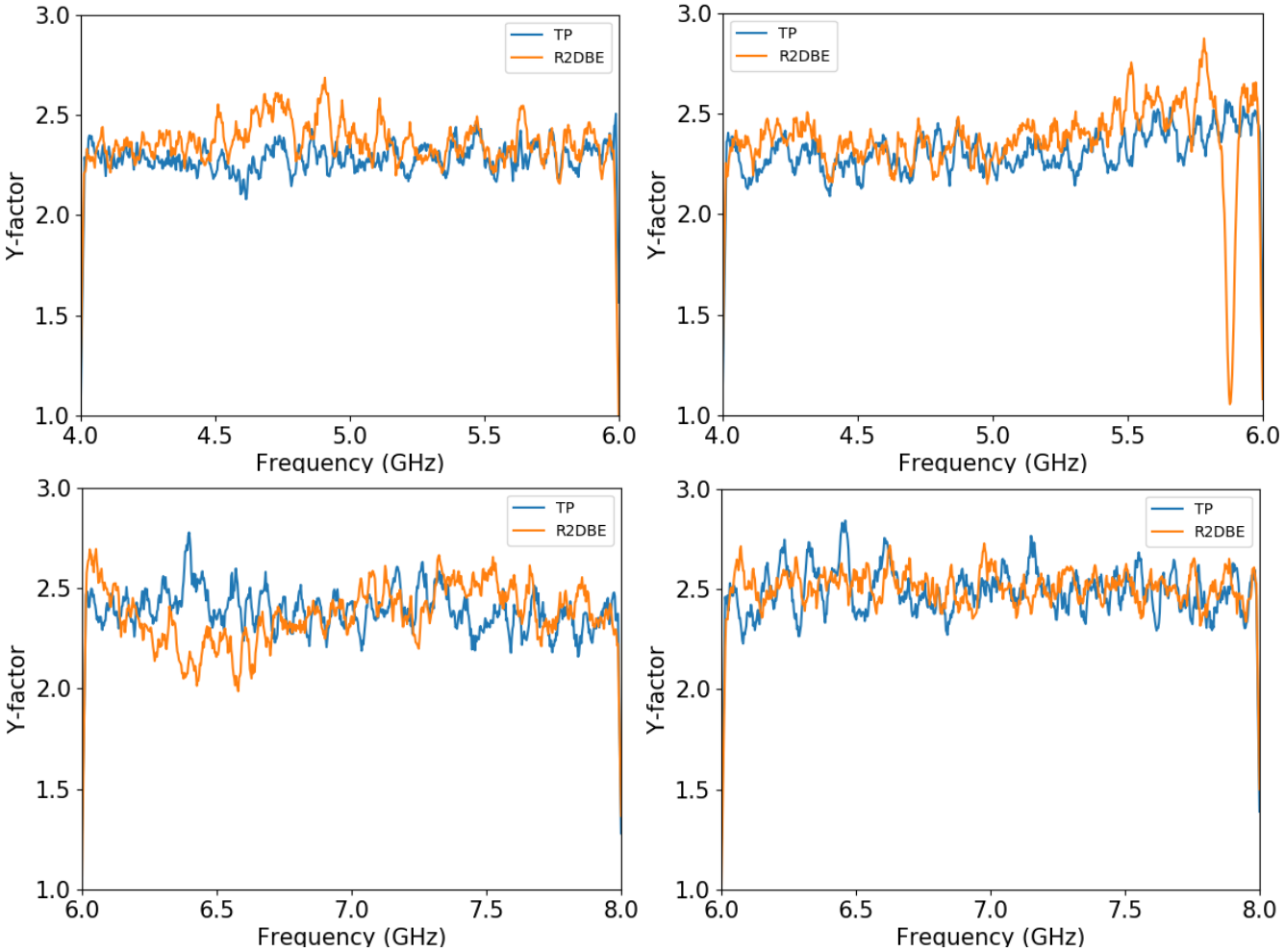


Figure 10: Spectral Y-factor at the receiver total-power box (in blue) and at the backend (input to the R2DBE; in orange), measured with the spectrum analyzer. *Top left:* low band LCP Y-factor. *Top right:* low band RCP Y-factor. *Bottom left:* high band LCP Y-factor. *Bottom right:* high band RCP Y-factor.

# 8 Updated Gain Curve for 2017

Telescopes are not perfectly rigid paraboloids, and must thus suffer some losses of signal due to distorted illumination of the main reflector as they slowly move to different elevations. This large-scale surface deformation affects the received signal and is not taken into account in the measurements leading to the efficiency and DPFU characterization. These losses can be determined by tracking sources over a wide elevation range, preferably as they increase and decrease in elevation from the tree-line to transit and vice-versa. An elevation-dependent gain curve for the telescope is measured, where the maximum (g = 1) is set where the telescope is expected to be most efficient. The gain curve is estimated by fitting a polynomial (usually second-order for standard radio-dishes). If more than one source is used, this is done once the flux density measurements are normalized around a plateau (to a relative gain scale). The source measurements used to obtain a gain curve must of course be calibrated for all other effects, including telescope efficiency (through the DPFU) and the atmospheric attenuation of the signal (through $T^*_{\rm sys}$).

Analogously to the previous runs in 2015 and 2016, continuum measurements were made at 1.3 mm of various non-variable calibrator sources. The elevation dependence was investigated using two non-variable sources tracked across the sky for a short period of time (10 hours over one night) and a wide range of elevations: K3-50, a planetary nebula; and W75N, a star formation region. This tracking was the best method to isolate the elevation-dependent component in the SMT output. The sources reached higher elevations but

disappeared at very low elevations behind the solar avoidance zone. The relative gain for the source measurements were taken using the ratio of the measurement against an average value of the upper envelope of data points in a mid-to-high elevation range where the measurements were constant – for a radio telescope, this typically occurs between 40 and 60$^o$. The effect of elevation on the relative gain can be clearly seen in Fig. 11.

The elevation-dependent geometric (opacity-free) gain curve can be constrained with little-to-no elevation effect from the atmosphere, an effect corrected by the $T^*_{\rm sys}$ measurements from the chopper calibration. It is best approximated as the second-order polynomial shown in Fig. 11. Relative error bars are obtained from the standard deviation of the non-corrected gain distribution around unity.

Observing was done in a similar manner to the 2016 gain curve, constraining the measurements to elevations above 20°. The gain curve for the SMT for 2017 is once again a typical radio-telescope elevation gain curve, with a plateau around 40-60°.

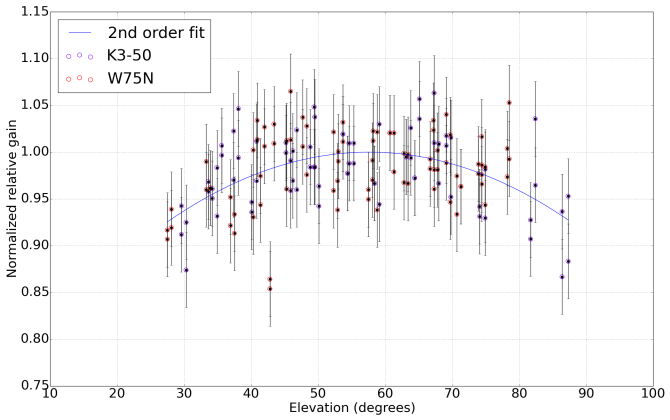


Figure 11: The best-fit second order polynomial to the relative gains of the two calibrator sources, K3-50 and W75N is used as the elevation-dependent gain curve.

The best fit parameters of the elevation-dependent gain curve (of the form $a_2(\mathrm{el})^2 + a_1(\mathrm{el}) + a_0$) are shown in Table 3 below[7]. These are consistent within the error margins with the coefficients of the gain curve for 2016 determined in Memo 2. This result is reassuring, as no work has been done on the telescope in the past year and so the gain curve was not expected to change.

Table 3: Gain fit parameters for the 2017 elevation curve.

| parameter | value |
|---|---|
| $a_0$ | $0.73 \pm 0.04$ |
| $a_1$ | $(0.9 \pm 0.1) \times 10^{-2}$ |
| $a_2$ | $(-0.8 \pm 0.1) \times 10^{-4}$ |

Following the constraint of the elevation gain curve $g(\mathrm{el})$, `LinuxPops` can contain the gain curve terms and incorporate them in the SMT calibration procedure in the following way, where the elevation is in degrees:

$$g = -0.8 \times 10^{-4}(\mathrm{el})^2 + 0.9 \times 10^{-2}(\mathrm{el}) + 0.73 \qquad (34)$$

The final flux density is then given by:

$$S = \frac{1}{\eta_{\rm A} g(\mathrm{el})} \frac{2k}{A_{\rm geom}} T^*_{\rm A} \qquad (35)$$

Table 4: Mean flux densities of most EHT observing targets (science targets and calibrators) at 228.1 GHz (1.3 mm) during the EHT+ALMA observing run in April 2017.

| Source name | Mean flux density [Jy] | ± Statistical uncertainty [Jy] |
|---|---|---|
| 3C84 | 11.4 | 0.3 |
| 3C273 | 7.2 | 0.2 |
| 3C279 | 8.5 | 0.2 |
| 3C345 | 2.3 | 0.1 |
| 0510+180 | 2.1 | 0.3 |
| BLLAC | 1.7 | 0.1 |
| CENA | 8.5 | 0.3 |
| M87 | 2.1 | 0.3 |
| OJ287 | 3.9 | 0.3 |
| SGRA | 9.0 | 0.6 |

# 9 SMT 1.3 mm Measurements

During the EHT+ALMA observing run in April 2017, flux density measurements were obtained for a number of EHT science targets and calibrator sources, by averaging multiple 2.7 min continuum ON-OFF scans in single-dish mode over the EHT observing window (April 4-12, 2017).

The cadence of single-dish observations was not constant or identical between all the sources: some sources were observed more frequently due to their availability during SMT

[7]More digits and the covariance matrix for the fit parameters can be obtained upon request.

off-time from the VLBI schedules. Table 4 below presents the mean flux densities for these observed sources during the EHT + ALMA observing run in April 2017. Not all EHT sources are present, some were not visible for long enough during the run to observe them separately with the SMT alone.

# 10 Conclusion

The April 2017 run gave the opportunity to re-evaluate every step of the calibration procedure for amplitude scaling for the SMT. A more detailed understanding of the calibration procedure for the telescope was obtained from previous memos, and enabled a more critical evaluation of the strategy currently used. Some limitations were found concerning the telescope DPFU and aperture efficiency: one of the key results of this memo is an updated estimate for the beam-width of 34.8 ± 0.6 arcseconds at 228 GHz, for a more accurate coupling of the planet calibrators to the telescope beam than in previous years. Furthermore, a more realistic estimation of the aperture efficiency was obtained, no differences in DPFU were found between the two polarizations, and measurements were quite consistent over the years, with no significant time-dependence detected.

A test of the signal loss in the VLBI backend was also done in 2017, to investigate the hypothesis that a possible discrepancy between the single-dish calibration information and the scaling needed for EHT data was due to attenuation of signal in the VLBI equipment. It was found, using the Y-factor test at the SMT total-power box, at the input to the R2DBE and within the R2DBE itself, that no signal loss was occuring and the Y-factor results were consistent with each other. It is therefore safe to assume that the single-dish calibration procedure should be suitable to calibrate SMT visibility amplitudes in EHT data in its entirety.

This memo also described the full procedure for the system temperature estimation via the chopper technique, using exact equations from the telescope software written by Tom Folkers. We confirmed that the output of the chopper technique is the effective system temperature $T^*_{\rm sys}$, which already corrects for atmospheric attenuation of the signal and rearward losses. The $T^*_{\rm sys}$ measurements are done before each VLBI scan, but the SMT additionally records total-power data that can be used to track intra-scan system temperature trends. This total-power data is available on the EHT wiki as part of the SMT logs for April 2017 observing.

The gain curve was also determined once more in 2017. The resulting fit parameters are consistent, within error estimates, with the curve measured in 2016 (Memo 2). This is an expected result as no work has been done on the telescope since, and it confirms the robustness of the method used to determine the gain curve.

The complete calibration procedure, when taking into account elevation-dependent gain from the gain curve and the newly determined DPFU, yields all the necessary calibration information for adequate antenna-based scaling of the visibility amplitudes from the SMT for EHT observations. For example, the calibration information is currently consistent with the necessary scaling done by Dr. Rusen Lu and Dr. Thomas Krichbaum for the amplitude calibration of the SMT baselines in EHT 2013 data.

There remains, however, a number of limitations in the calibration procedure that should be investigated further in the future. The beam-width estimation, although adequate considering the uncertainty in pointing and focus dominates the DPFU analysis, is still not quite accurate. We have assumed that the SMT has a circular beam, but from the Gaussian fits it appears to be elliptical instead. A more accurate fit of the Jupiter maps, such as fitting both beams simultaneously or fitting a convolution of the planet disk and a Gaussian instead of a simple Gaussian would yield better results. Another limitation in the calibration is the chopper procedure: the assumption that the vane temperature is the same as the ambient temperature is likely incorrect, as the vane was moved from the receiver cabin (which is at around ambient temperature) to a room in the telescope building (which is closer to room temperature). Some additional assumptions, such as whether the sideband ratio is indeed negligible, must also be looked at more carefully. The chopper technique itself also has its own limitations outside of telescope-specific assumptions. Nevertheless, the current method should yield suitable results for the calibration of EHT observations.

# Acknowledgements

This work is supported by the ERC Synergy Grant BlackHoleCam: Imaging the Event Horizon of Black Holes (Grant 610058). D.P.M., J.K. and T.W.F. receive support via NSF MSIP award AST-1440254.

## Useful References


Altenhoff, W.J., *The Solar System: (Sub)mm Continuum Observations*, Proceedings of the ESO-IRAM-Onsala Workshop on (Sub)Millimeter Astronomy, 1996.

Bach, U., *Seminar: Pointing and Single Dish Amplitude Calibration Theory*, Max Planck Institut für Radioastronomie.

Baars, J.W.M., *The Measurement of Large Antennas with Cosmic Radio Sources*, IEEE Transactions on Antennas and Propagation, Vol. AP-21, No. 4, July 1973.

Baars, J.W.M., *The paraboloidal reflector antenna in radio astronomy*, Springer, 2007.

Bensch F., Stutzki S., Heithausen A., *Methods and constraints for the correction of error beam pick-up in single dish radio observations*, A&A **365**, 285-293 (2001).

Berdahl P., Fromberg R., *The Thermal Radiance of Clear Skies*, Solar Energy, Vol. 29, No. 4, pp. 299-314, 1982.

Berdahl P., Martin M., *Technical Note: Emissivity of clear skies*, Solar Energy, Vol. 32, No. 5, pp. 663-664, 1984.

Berger X., Buriot D., Garnier F., *About the Equivalent Radiative Temperature for Clear skies*, Solar Energy, Vol. 32, No. 6, pp. 725-733, 1984.

Burke B.F., Graham-Smith F., *An Introduction to Radio Astronomy*, 1997, Cambridge University Press.

Cappellen, W. van, *Efficiency and sensitivity definitions for reflector antennas in radio-astronomy*, ASTRON, SKADS MCCT Workshop, 26-30 November 2007.

Gordon M.A., Baars J.W.M., Cocke W.J., *Observations of radio lines from unresolved sources: telescope coupling, Doppler effects, and cosmological corrections*, A&A **264**, 337-344 (1992).

Greve A., Bremer M., *Thermal Design and Thermal Behavior of Radio Telescopes and their Enclosures*, Chapter 4, Section 7, Springer, 2010.

Kraus, A., *Calibration of Single-Dish Telescopes*, Max Planck Institut für Radioastronomie, ERATec-Workshop - Bologna, 28 October 2013.

Kramer, C., *Calibration of spectral line data at the IRAM 30m radio telescope*, Version 2.1, IRAM, January 24th 1997.

Kramer, C., *Millimeter Calibration*, presentation at IRAM Summer School 2013, IRAM, Granada, Spain.

Kraus, J.D., *Radio Astronomy*, 1986, Cygnus-Quasar Books, Powell OH.

Iguchi, S., *Radio Interferometer Sensitivities for Three Types of Receiving Systems: DSB, SSB and 2SB Systems*, PASJ **57**, 643-677, August 2005.

Issaoun .S, Folkers T.W., Blackburn L., et al. *A conceptual overview of single-dish absolute amplitude calibration*, EHT Memo 2017-CE-01, 2017.

Mangum, J.G., *Equipment and Calibration Status for the NRAO 12 Meter Telescope*, National Radio Astronomy Observatory, September 1999.

Mangum, J.G., *Main-Beam Efficiency Measurements of the Caltech Submillimeter Observatory*, Publ. of the Astron. Soc. of the Pacific **105**, 116-122, January 1993.

Martí-Vidal I., Krichbaum T.P., Marscher A. et al. *On the calibration of full-polarization 86 GHz global VLBI observations*, A&A, **542**, A107 (2012).

O'Neil, K., *Single Dish Calibration Techniques at Radio Wavelengths*, NAIC/NRAO School on Single Dish Radio Astronomy, ASP Conference Series, 2001, Salter, et al.

Pardo J.R., Cernicharo J., Serabyn E., *Atmospheric Transmission at Microwaves (ATM): An Improved Model for Millimeter/Submillimeter Applications*, IEEE Transactions on Antennas and Propagation, Vol. 49, No. 12, December 2001.

Rohlfs, K., *Tools of Radio Astronomy*, 1986, Springer-Verlag: Berlin, Heidelberg.

Ruze, J., *The Effect of Aperture Errors on the Antenna Radiation Pattern*, Il Nuovo Cimento Volume 9, Supplement 3, pp 364-380, March 1952.

Sandell, G., *Secondary calibrators at submillimetre wavelengths*, Mon. Not. R. Astron. Soc. **271**, 75-80 (1994).

Thompson A.R., Moran J.M., Swenson G.W., *Interferometry and Synthesis in Radio Astronomy*, 1986, John Wiley and Sons; New York.

Tournaire, A., *Controle thermique du telescope et du batiment*, Themis, INSU/TECH/AT/CT/No86/8, France (1986).

P.R. Bevinson and D.K. Robinson.*Data Reduction and Error Analysis.* McGraw Hill, 2003.

# A Variables in LinuxPops

In this memo, the variables for the LinuxPops and telescope calibration techniques were introduced. However, in the programs, some variables are called differently. Below is a table with the different variables introduced and their respective LinuxPops or atm.c (telescope calibration script) symbol.

Table 5: Calibration variables in LinuxPops and atm.c

| variable name | symbol in calibration procedure | symbol in LinuxPops or atm.c |
|---|---|---|
| elevation | El | El |
| hot load counts | $C_{\text{hot}}$ | Thot |
| blank sky counts (for system temp) | $C_{\text{sky}}$ | Tsky |
| cold load counts | $C_{\text{cold}}$ | Tcold |
| vane (hot load) temperature | $T_{\text{vane}}$ | Tvane |
| cold load temperature | $T_{\text{cold}}$ | TCOLD |
| receiver noise temperature | $T_{\text{rx}}$ | Trx |
| ambient temperature | $T_{\text{amb}}$ | Tamb |
| atmospheric emission temperature | $T_{\text{em}}$ | Tem |
| atmospheric emission temperature in image band | $T_{\text{em,i}}$ | Temi |
| atmospheric emission temperature in signal band | $T_{\text{em,s}}$ | Tems |
| cabin temperature | $T_{\text{cab}}$ | Tcab |
| forward efficiency | $\eta_{\text{eff}}$ | be_eff |
| sideband ratio | $r_{\text{sb}}$ | sbr |
| counts on-source | $C_{\text{on}}$ | Sig |
| counts off-source (for observing) | $C_{\text{sky}}$ | Sky |
| signal-to-noise ratio | $\frac{S-N}{N}$ | $\frac{Sig-Sky}{Sky}$ |
| calibration temperature | $T_{\text{cal}}$ | Tcal |
| effective system noise temperature | $T^*_{\text{sys}}$ | Tsys |
| opacity corrected antenna temperature | $T^*_{\text{A}}$ | Ta* |
| sky opacity at the zenith | $\tau_0$ | Tau |
| sky opacity at the zenith in signal band | $\tau_{0,s}$ | taus |
| atmospheric attenuation factor | $e^{\tau_0 * AM}$ | TauEL |
| elevation gain correction factor | $\frac{1}{G}$ | GainEL |
| efficiency correction factor | $\frac{1}{\eta_{\text{A}}}$ | Fac |
| calibrated antenna (resistor) temperature | $T_{\text{R}}$ | Tr |
| flux density | $S$ | Jy's |